

## PHYSICS

## Current-induced dynamics of skyrmion strings

Tomoyuki Yokouchi<sup>1,\*†</sup>, Shintaro Hoshino<sup>2,\*</sup>, Naoya Kanazawa<sup>1</sup>, Akiko Kikkawa<sup>2</sup>,  
Daisuke Morikawa<sup>2</sup>, Kiyou Shibata<sup>2</sup>, Taka-hisa Arima<sup>2,3</sup>, Yasujiro Taguchi<sup>2</sup>,  
Fumitaka Kagawa<sup>2</sup>, Naoto Nagaosa<sup>1,2</sup>, Yoshinori Tokura<sup>1,2†</sup>

Dynamics of string-like objects is an important issue in a broad range of physical systems, including vortex lines in superconductors, viscoelastic polymers, and superstrings in elementary particle physics. In noncentrosymmetric magnets, string forms of magnetic skyrmions are present as topological spin objects, and their current-induced dynamics has recently attracted intense interest. We show in the chiral magnet MnSi that the current-induced deformation dynamics of skyrmion strings results in transport response associated with the real-space Berry phase. Prominent nonlinear Hall signals emerge above the threshold current only in the skyrmion phase. We clarify the mechanism for these nonlinear Hall signals by adopting spin density wave picture to describe the moving skyrmion lattice; deformation of skyrmion strings occurs in an asymmetric manner due to the Dzyaloshinskii-Moriya interaction, which leads to the nonreciprocal nonlinear Hall response originating from an emergent electromagnetic field. This finding reveals the dynamical nature of string-like objects and consequent transport outcomes in noncentrosymmetric systems.

## INTRODUCTION

Topologically stable defects cannot be unwound by continuous transformation or weak perturbations (1). As for string-like topological defects, topological stability determines the degree of freedom of bends; for example, when part of a string is pulled, the string does not break but flexibly deforms. Because of this nature, the string-like topological defects exhibit rich forms and dynamical properties. One of the most prototypical examples is vortex lines in type II superconductors (SCs); aggregates of vortex lines form various states, such as the glass state and the liquid state, depending mainly on the relative strength of the pinning force, thermal fluctuations, and the energy cost of bending vortex lines (2). Moreover, deformations are also dynamically induced by external forces such as electrical current (3).

Recently, a string-like topological defect has been found in spin systems, that is, skyrmion strings (4–8). A skyrmion string is a vortex-like topological spin structure 5 to 200 nm in diameter and 10 to 10,000  $\mu\text{m}$  in length along the external magnetic field direction, emerging in noncentrosymmetric magnets because of competition between ferromagnetic exchange interaction and the Dzyaloshinskii-Moriya (DM) interaction. The topological nature of skyrmions, characterized by a topological number of  $-1$ , not only guarantees their stability against weak perturbations but also produces unique transport phenomena related to the real-space Berry phase, which acts as an emergent electromagnetic field to conduction electrons (7, 8), such as the topological Hall effect (9), low current drive (10), and the consequent emergent electric field analogous to electromagnetic induction (11). In particular, the latter has inspired research studies on skyrmion-based memory device applications (12). However, in previous research studies on current-induced translational motion, skyrmion strings were treated as two-dimensional objects or straight cylinders, and the degree of freedom of the deformation of skyrmion strings (that is, flexibility) was ignored. In reality, a skyrmion string has a flexible nature as in the case of the vortex line. Hence, especially under translational motion

in the presence of random impurities, skyrmion strings should dynamically deform to avoid impurities (Fig. 1A). This assumption is based on simulations in a two-dimensional system (13), according to which a translationally moving skyrmion is deformed to avoid impurities; it is natural to extend the concept of the deformation to a skyrmion string in a three-dimensional system. We note that current-induced dynamics of skyrmion strings in a three-dimensional system has also been simulated to find flexible deformation of the strings (14). In this study, we investigate current-induced deformation dynamics of skyrmion strings arising from this flexibility. To this end, we focus on the nonlinear Hall effect, which is empirically known as a sensitive probe for current-induced spin dynamics in noncentrosymmetric systems (15). In the following, we demonstrate that skyrmion strings asymmetrically deformed because of their flexible nature and the DM interaction, consequently giving rise to a nonreciprocal nonlinear Hall response originating from an emergent electromagnetic field.

## RESULTS AND DISCUSSION

B20-type MnSi has a noncentrosymmetric lattice structure, which can exist in two enantiomeric forms: right- and left-handed structures. From the viewpoint of symmetry, the nonreciprocal nonlinear Hall electric field ( $E_z$ ) in MnSi can be described as follows

$$E_z = \alpha(j_x, B_z)j_x \quad (1)$$

Here,  $j_x$  and  $B_z$  are the  $x$  component of current density and the  $z$  component of magnetic field, respectively, and the nonreciprocal nonlinear Hall coefficient  $\alpha(j_x, B_z)$  is pseudoscalar, which is an odd function of  $j_x$  and  $B_z$  (Fig. 1A). The nonreciprocal response in the nonlinear transport phenomenon is defined as different responses to positive and negative currents ( $\pm j$ ) when viewed from the current direction. A direction of the nonlinear Hall electric field is parallel or antiparallel to  $B_z$ , depending on crystal chirality (see also the Supplementary Materials). We fabricated microscale MnSi thin plates by using a focused ion beam (FIB) (Fig. 1B) to increase current density under the limitations of external high-precision current sources. The crystal chirality was determined by using convergent beam electron

Copyright © 2018  
The Authors, some  
rights reserved;  
exclusive licensee  
American Association  
for the Advancement  
of Science. No claim to  
original U.S. Government  
Works. Distributed  
under a Creative  
Commons Attribution  
NonCommercial  
License 4.0 (CC BY-NC).

<sup>1</sup>Department of Applied Physics, The University of Tokyo, Tokyo 113-8656, Japan.

<sup>2</sup>RIKEN Center for Emergent Matter Science, Wako 351-0198, Japan. <sup>3</sup>Department of Advanced Materials Science, The University of Tokyo, Kashiwa 277-8561, Japan.

\*These authors contributed equally to this work.

†Corresponding author. Email: yokouchi@cmr.t.u-tokyo.ac.jp (T.Y.); tokura@riken.jp (Y.T.)

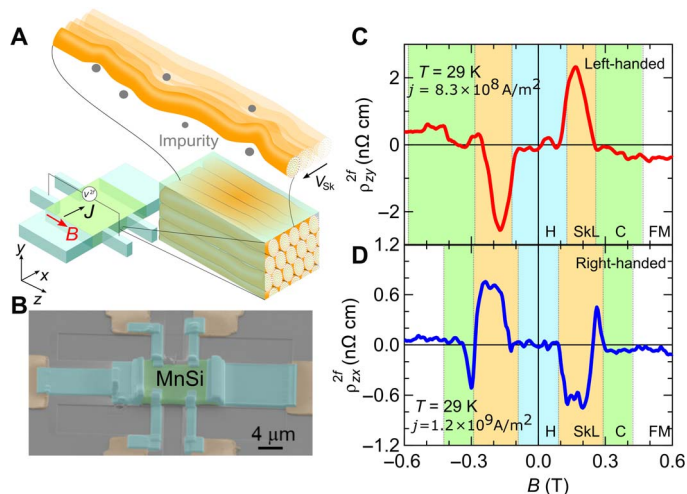


**Fig. 1. Experimental configurations and the second-harmonic Hall effect in MnSi.** (A) Schematic picture of translationally moving skyrmion strings and the experimental setup for second-harmonic Hall measurement. (B) Scanning electron microscope image of a MnSi thin-plate sample: MnSi crystal (green), gold electrodes (yellow), tungsten (light blue) to fix the MnSi and to connect the gold electrodes to MnSi, and a silicon stage (gray). (C and D) Magnetic field dependence of second-harmonic Hall resistivity ( $\rho_{zx}^{2f}$ ) in right-handed (C) and left-handed (D) MnSi crystals. The blue, orange, green, and white shadows represent helical (H), SkL, conical (C), and ferromagnetic (FM) phases, respectively.

diffraction (CBED) (16, 17). To detect nonlinear Hall signals, we performed second-harmonic measurement; we input low-frequency sine-wave AC and measured the real and imaginary parts of second-harmonic complex resistivity ( $\text{Re } \rho_{zx}^{2f}$  and  $\text{Im } \rho_{zx}^{2f}$ ), which are directly linked to the nonreciprocal nonlinear Hall coefficient (see the Supplementary Materials). First, we show typical profiles of the second-harmonic Hall effect. As shown in Fig. 1 (C and D), the  $B$  dependence of  $\text{Re } \rho_{zx}^{2f}$  of both right- and left-handed crystals exhibits prominent enhancement in the skyrmion lattice (SkL) phase, in which the skyrmion strings form a triangular lattice (see Fig. 1A for the schematic). The signs of  $\text{Re } \rho_{zx}^{2f}$  are reversed between right- and left-handed crystals, in accordance with the expected contributions from the nonreciprocal nonlinear Hall effect. Figure 2A shows the  $B$  dependence of  $\text{Re } \rho_{zx}^{2f}$  in the left-handed MnSi crystal with current densities  $j = 2.1 \times 10^8$  A/m $^2$  (blue lines) and  $j = 8.3 \times 10^8$  A/m $^2$  (red lines) at various temperatures. The magnitude of  $\text{Re } \rho_{zx}^{2f}$  measured with  $j = 2.1 \times 10^8$  A/m $^2$  is small enough below noise levels. In contrast, in the case of  $\text{Re } \rho_{zx}^{2f}$  measured with  $j = 8.3 \times 10^8$  A/m $^2$ , the prominent signals of  $\text{Re } \rho_{zx}^{2f}$  are observed in the skyrmion phase. The clear correspondence between the SkL phase and the conspicuous  $\text{Re } \rho_{zx}^{2f}$  signals is further confirmed in the contour map of  $\text{Re } \rho_{zx}^{2f}$  with  $j = 8.3 \times 10^8$  A/m $^2$  in the  $T$ - $B$  phase diagram (Fig. 2B; see the Supplementary Materials for the determination of the magnetic phase diagram).

To gain more insight, we measured the detailed current-density dependence of  $\rho_{zx}^{2f}$ . Taking into account the increase in sample temperature owing to Joule heating, we derived the temperature from the longitudinal resistivity of the thin-plate sample itself and adjusted the temperature of the heat bath so that the sample temperature remained constant. Figure 3A shows the current-density dependence of the temperature of the sample, demonstrating that the temperature ( $T$ ) of the sample remained nearly constant within the  $29.0 \pm 0.08$  K range. The current-density dependence of  $\text{Re } \rho_{zx}^{2f}$  at  $T = 29$  K

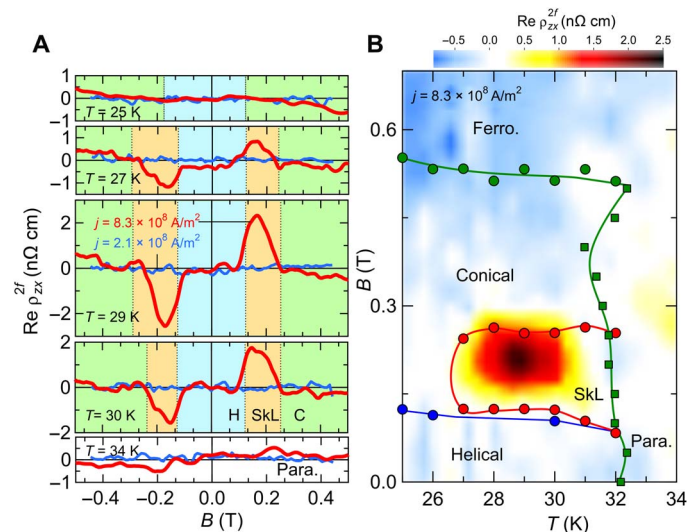


**Fig. 2. The second-harmonic Hall effect near the transition temperature.** (A) Magnetic field dependence of the real part of second-harmonic Hall resistivity ( $\text{Re } \rho_{zx}^{2f}$ ) measured with current densities  $j = 2.1 \times 10^8$  A/m $^2$  (blue lines) and  $j = 8.3 \times 10^8$  A/m $^2$  (red lines). The blue, orange, green, and white shadows represent helical, SkL, conical, and ferromagnetic phases, respectively. (B) Contour mapping of  $\text{Re } \rho_{zx}^{2f}$  in the temperature-magnetic field plane. The blue, green, and red circles denote helical-to-conical, conical-to-ferromagnetic, and SkL-to-conical phase transitions, respectively, determined from kinks in the magnetic field dependence of planar linear Hall resistivity. The green squares represent helical, conical, and SKL-to-paramagnetic phase transitions determined from inflection points of the temperature dependence of longitudinal resistivity (see also the Supplementary Materials).

measured by using sine-wave AC with  $f = 13$  Hz exhibits a nonmonotonous profile (Fig. 3B). Here, we note that the current-density dependence measured by using sine-wave AC and square-wave current is almost identical. This result rules out the possibility that the nonmonotonous current dependence results from a temporal temperature change, which would possibly occur in the case of sine-wave AC but not in the case of square-wave current (see also the Supplementary Materials). The profile of the current-density dependence of  $\text{Re } \rho_{zx}^{2f}$  is divided into three distinct regimes: (i) almost zero below  $j_{\text{th}} = 3.2 \times 10^8$  A/m $^2$ , (ii) monotonic increase between  $j_{\text{th}}$  and  $j_{\text{CO}} = 8.9 \times 10^8$  A/m $^2$ , and (iii) monotonic decrease above  $j_{\text{CO}}$ . This indicates that the nature of the SkL state changes with increasing current density. These changes are widely observed in charge density wave (CDW) (18, 19) and SC vortices (20, 21): (i) pinned lattice state at low current densities, (ii) disordered flow of lattice affected by the pinning potential in intermediate current densities, and (iii) recovery of crystallinity due to motional narrowing, that is, relative reduction of the pinning force, at large current densities, termed dynamical reordering. Such a dynamical phase diagram is also theoretically predicted for SkL in the presence of a strong random pinning potential (22). On the basis of this theoretical prediction and the analogousness to dynamical phase diagrams of CDW and SC vortices, we assign  $j_{\text{th}}$  and  $j_{\text{CO}}$  to the onset of disordered translational motion and dynamical reordering of skyrmion strings, respectively. Note that  $j_{\text{th}}$  corresponds to the dynamical phase transition point, while  $j_{\text{CO}}$  characterizes the crossover (CO). The temperature dependences of  $j_{\text{th}}$  and  $j_{\text{CO}}$  (Fig. 3C) are also consistent with the above assignment;  $j_{\text{th}}$  and  $j_{\text{CO}}$  decrease with increasing temperature because thermal activation effectively weakens the pinning force. Therefore, a plausible scenario accounting for the nonmonoto-

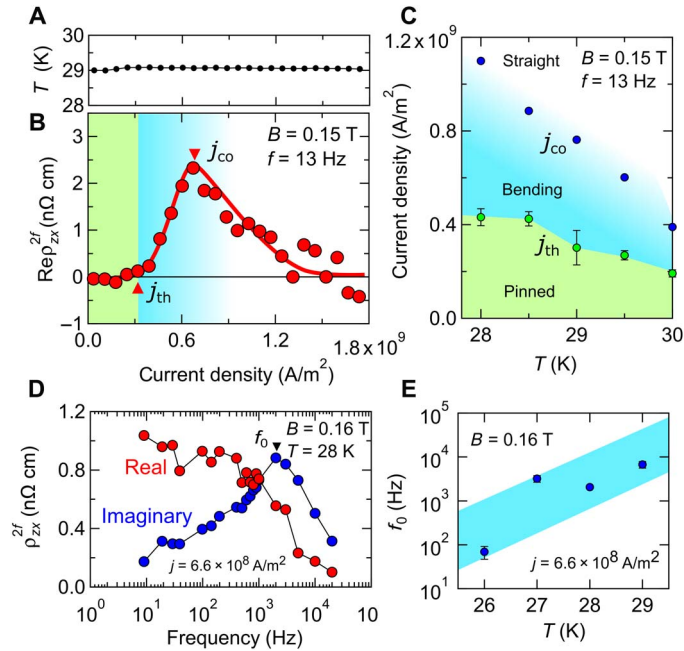


**Fig. 3. Current density and frequency dependence of the second-harmonic Hall effect.** (A and B) Current density ( $j$ ) dependence of the temperature of the MnSi thin-plate sample estimated from longitudinal resistivity (A) and the real part of second-harmonic Hall resistivity ( $\text{Re}\rho_{zx}^{2f}$ ) at  $B = 0.15$  T measured with the frequency  $f = 13$  Hz (B). The red solid curve is a guide to the eyes. (C) Temperature dependence of threshold current densities  $j_{\text{th}}$  and the crossover point  $j_{\text{CO}}$  at  $B = 0.15$  T. The values of  $j_{\text{th}}$  and  $j_{\text{CO}}$  at  $T = 29.0$  K are represented as triangles in (B). (D) Dependence of the real part (line with red dots) and the imaginary part (line with blue dots) of  $\rho_{zx}^{2f}$  on the input current frequency at  $T = 28$  K and  $B = 0.16$  T. (E) Temperature dependence of frequency ( $f_0$ ), where the imaginary part of  $\rho_{zx}^{2f}$  peaks. The  $f_0$  values at  $T = 28$  K are represented by the inverse triangle in (D). The thick light blue band is a guide to the eyes.

nous current dependence of  $\rho_{zx}^{2f}$  is that the translational motion of deformed skyrmion strings occurs at current densities between  $j_{\text{th}}$  and  $j_{\text{CO}}$ , leading to the second-harmonic Hall signal along the  $B$  direction. We note that the critical current density required for the translational motion of SkL,  $j_{\text{th}} = 3.2 \times 10^8$  A/m<sup>2</sup>, is two orders of magnitude larger than that reported for bulk MnSi (10, 11). This is perhaps due to the chemical disorder/strain on the wide top and bottom surfaces of the sample plate (see Fig. 1A) caused by the device fabrication procedure, which involved focused ion (Ga ion) beams, which act as additional pinning sites for skyrmion strings.

The close relationship between the second-harmonic Hall effect and the translational motion of skyrmion strings is further confirmed by the dependence of  $\rho_{zx}^{2f}$  on the input-current frequency. In Fig. 3D, we show the frequency dependence of  $\text{Re}\rho_{zx}^{2f}$  and  $\text{Im}\rho_{zx}^{2f}$  measured with  $j = 7.0 \times 10^8$  A/m<sup>2</sup> at  $T = 28$  K. At around  $f = 3$  kHz,  $\text{Re}\rho_{zx}^{2f}$  shows a rapid decrease together with the  $\text{Im}\rho_{zx}^{2f}$  peak, and both  $\text{Re}\rho_{zx}^{2f}$  and  $\text{Im}\rho_{zx}^{2f}$  are almost zero above  $f = 6$  kHz. This nonmonotonous frequency dependence in the present frequency range ( $f < 10$  kHz) could not be explained by conventional mechanisms of the second-harmonic Hall effect, such as spin-orbit torque (15) or asymmetric electron-magnon scattering (23), with typical frequencies of several gigahertz. Because the characteristic frequency in motion of nanoscale spin structures such as ferromagnetic domain walls is below several megahertz (24), the observed frequency dependence can be interpreted as representing the relationship between  $\rho_{zx}^{2f}$  and the translational motion of skyrmion

strings; skyrmion strings cannot follow the AC with a frequency ( $f$ ) above 6 kHz. The profile of the observed frequency dependence of  $\rho_{zx}^{2f}$  resembles that of the skyrmion velocity ( $v_{\text{Sk}}$ ) derived from Thiele's equation (see the Supplementary Materials). Additionally, as shown in Fig. 3E, the frequency ( $f_0$ ) at which  $\text{Im}\rho_{zx}^{2f}$  peaks increases with increasing temperature. Because skyrmion strings can be driven faster at higher temperatures owing to the assistance of thermal activation, the temperature dependence of  $f_0$  also reasonably supports the relationship between  $\rho_{zx}^{2f}$  and the translational motion of SkL.

To clarify the dominant mechanism of the nonlinear Hall signal along the  $B$  direction, we calculate the current-induced dynamics of skyrmion strings and the consequent emergent electromagnetic field in the presence of impurity potentials. The model corresponds to experimental situations in which skyrmion strings flow while accompanying distortions (that is,  $j_{\text{th}} < j < j_{\text{CO}}$ ). In the following, we demonstrate that the experimental observation is well explained in terms of the current-driven asymmetric deformation dynamics of skyrmion strings and the consequent generation of the emergent electromagnetic field. On the basis of the spin density wave picture, the spin texture for SkL is given by the triple-helix state with the modulated phase in space-time (4, 7, 25). This deformation corresponds to the low-lying spin-wave excitation modes of SkL, namely, phasons (25). The response function for phasons is calculated from the energy cost of the deformation based on the DM ferromagnetic Hamiltonian in the presence of impurities (26)

$$H = \int \frac{d\mathbf{r}}{a^3} \left[ \frac{1}{2} J a^2 (\nabla \mathbf{n})^2 + D \mathbf{a} \mathbf{n} \cdot (\nabla \times \mathbf{n}) - g \mu_B \mathbf{B} \cdot \mathbf{n} \right] + \int \frac{d\mathbf{r}}{e^3} V(\mathbf{r})(n^z)^2 \quad (2)$$

where the first, second, third, and fourth terms are Heisenberg interaction, DM interaction, Zeeman term, and impurity potential, respectively. The length  $\ell$  ( $>$  lattice constant  $a$ ) is the average distance between impurities, and the inverse of skyrmion radii is given by  $Q = |D|/(Ja)$  in this model. Combining the above Hamiltonian with the Berry phase term in the action, we derive a dynamical response function (see Materials and Methods). The excitation energy  $\epsilon(\mathbf{q})$  of SkL, which is determined from the pole of the response function, has the following form (27):  $\epsilon(\mathbf{q}) = \alpha \mathbf{q}^2 + \beta \mathbf{q}^4 + \gamma \mathbf{q}^4 q_z + O(q^6)$  (Fig. 4A). The third term with  $q_z$  shows non-reciprocity of skyrmion string dynamics along the  $z$  direction, which is crucial to the nonlinear Hall effect, as shown in the following.

First, to provide an intuitive picture of the current-induced string dynamics in the presence of impurities and consequent emergent electromagnetic fields, we focus on a flowing single skyrmion string bent to avoid an impurity as a representative example of deformed skyrmion strings. Bending of the skyrmion string is described by the displacement vector  $\mathbf{u} = (u_x, u_y, 0)$  (Fig. 4C), and the Hall electric field originating from emergent magnetic and electric fields is given by  $\mathbf{e} + (\mathbf{v}_e - \mathbf{v}_{\text{Sk}}) \times \mathbf{b}$ , where  $\mathbf{v}_e = v_e \hat{\mathbf{x}}$  and  $\mathbf{v}_{\text{Sk}} = v_{\text{Sk}} \hat{\mathbf{x}}$  are the velocity of electrons and skyrmions ( $v_{\text{Sk}} \lesssim v_e$ ) and  $\mathbf{e} = -\dot{\mathbf{u}} \times \mathbf{b}$  and  $(\mathbf{v}_e - \mathbf{v}_{\text{Sk}}) \times \mathbf{b}$  are the emergent electric field and the topological Hall electric field in the moving frame of skyrmions, respectively (see also the Supplementary Materials). As shown in Fig. 4 (C and F), the electric field  $E_z$  along the magnetic field direction is nonzero only when a skyrmion string bends. For a detailed investigation of electric fields along the  $B$  direction arising from current-induced dynamical bending, we calculate the time evolution of the bending skyrmion string by using  $\epsilon(\mathbf{q})$  and its eigenmode and the concomitant magnitude of  $[(\mathbf{v}_e - \mathbf{v}_{\text{Sk}}) \times \mathbf{b}]_z$  and  $-\dot{\mathbf{u}} \times \mathbf{b}_z$  (see the Supplementary Materials for detailed calculations). Figure 4 (D and G)



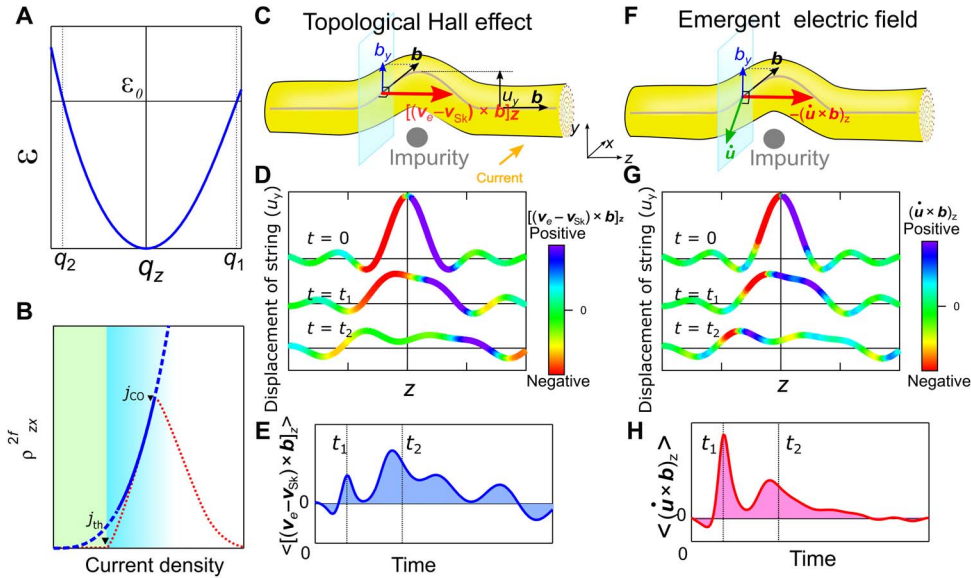


**Fig. 4. Emergent electromagnetic fields for dynamically generated deformed skyrmion strings.** (A) Dispersion relation of the low-energy excitation ( $\epsilon$ ) of SkL with a propagating vector along the external magnetic field direction ( $q_z$ ). (B) Schematic for the current density dependence of nonreciprocal nonlinear (second-harmonic) Hall resistivity. The solid blue line represents the theoretical calculation, which is valid for the current density between  $j_{th}$  and  $j_{CO}$ , and the broken blue line denotes the square of the current density and is simply a guide to the eyes. The red line indicates the experimentally observed current profile (see also Fig. 3B). (C and F) Schematics of emergent electromagnetic fields for the deformation of a skyrmion string when it collides with point-like impurity.  $\mathbf{u}$  represents the displacement vector of a skyrmion string. The red arrows denote the  $z$  components of the topological Hall electric field  $[(\mathbf{v}_e - \mathbf{v}_{Sk}) \times \mathbf{b}]_z$  (C) and the emergent electric field  $\mathbf{e}_z = -[\dot{\mathbf{u}} \times \mathbf{b}]_z$  (F). (D and G) Position ( $z$ ) dependence of the displacement of skyrmion strings shown together with the color map of the  $z$  components of both  $(\mathbf{v}_e - \mathbf{v}_{Sk}) \times \mathbf{b}$  (D) and  $\mathbf{e} = -\dot{\mathbf{u}} \times \mathbf{b}$  (G) at several time points. (E and H) Time dependence of the average  $z$  components of both  $(\mathbf{v}_e - \mathbf{v}_{Sk}) \times \mathbf{b}$  (E) and  $\mathbf{e} = -\dot{\mathbf{u}} \times \mathbf{b}$  (H) over the skyrmion string.

shows the time evolution of a bending skyrmion string shown together with the color map of the magnitude of  $[(\mathbf{v}_e - \mathbf{v}_{Sk}) \times \mathbf{b}]_z$  and  $-[\dot{\mathbf{u}} \times \mathbf{b}]_z$ , respectively, and Fig. 4 (E and H) shows the time dependence of their averages over the skyrmion string. At the initial state ( $t = 0$ ), because deformation is symmetric, both  $[(\mathbf{v}_e - \mathbf{v}_{Sk}) \times \mathbf{b}]_z$  and  $-[\dot{\mathbf{u}} \times \mathbf{b}]_z$  cancel out. With increasing time, however, the skyrmion string asymmetrically deforms because of the nonreciprocity of the dispersion  $\epsilon(\mathbf{q})$ , which leads to the nonzero average of  $E_z$ . The above intuitive picture thus indicates asymmetric deformation of skyrmion strings; therefore, the emergent electromagnetic fields play a crucial role in the nonreciprocal nonlinear Hall signal along the  $B$  direction.

Next, to gain more insight, we calculate the nonreciprocal response in SkL. Here, we note that the deformations of skyrmion strings are described as collective excitations, which include other types of deformations in addition to the bending deformation. The dynamical spin texture generates emergent electromagnetic fields that are given in the laboratory frame by (28, 29)

$$b_\mu = \frac{\hbar}{2e} \sum_{\nu\lambda} \epsilon_{\mu\nu\lambda} \mathbf{n} \cdot (\partial_\nu \mathbf{n} \times \partial_\lambda \mathbf{n}) \quad (3)$$

$$e_\mu = \frac{\hbar}{e} \mathbf{n} \cdot (\partial_\mu \mathbf{n} \times \partial_t \mathbf{n}) \quad (4)$$

The Hall electric field in the DC limit is

$$\mathbf{E}^{DC} = \lim_{T \rightarrow \infty} \int_{-T}^T \frac{dt}{2T} \int \frac{d\mathbf{r}}{\Omega} P(\mathbf{e}(\mathbf{r}, t) + \mathbf{v}_e \times \mathbf{b}(\mathbf{r}, t)) \quad (5)$$

where  $\Omega$  is the volume of the system,  $P$  is the spin polarization of the conduction electron at the Fermi level, and the angle bracket denotes

the impurity average. We expand the expression with respect to the impurity potentials (see Materials and Methods). After some calculations, we obtain the leading-order contribution to the nonlinear Hall resistivity defined by  $E_z^{DC} = \rho_{zx}^{DC} j_x$

$$\rho_{zx}^{DC} \sim \frac{P^2 \hbar a}{e^2} \cdot \frac{(\frac{\hbar a^2}{e} j_c)^3}{J^2 D} \left( \frac{j}{j_c} \right)^2 \quad (6)$$

where the electrical current is given by  $j = en_e v_e$ , with  $n_e \sim a^{-3}$  denoting electron density. Here, critical current density ( $j_c$ ) can be described by the impurity potential in Eq. 2 (see Materials and Methods). From Eq. 6, the sign of  $D$ , which depends on crystal chirality, corresponds to the sign of nonreciprocal nonlinear Hall resistivity, which is consistent with experimental observations (Fig. 1, C and D). We take the following parameters for MnSi (30):  $a \approx 2.9 \text{ \AA}$ ;  $J = J_0 S^2$ , with  $J_0 \approx 150 \text{ K}$  being the Heisenberg exchange at  $T = 0$  and with the helical spin moment  $S = 0.02$  taken near the transition temperature;  $D = 0.1J$ ; and  $P \approx 0.1$ . We have roughly estimated the typical value at  $j = 2j_c$  by using Eq. 6 as  $\rho_{zx}^{DC} \approx 0.4 \text{ n}\Omega \text{ cm}$ , which is comparable to the experimental values.

Although Eq. 6 is valid in the disordered skyrmion flowing regime at the current density with  $j_{th} < j < j_{CO}$  (see also the broken line in Fig. 4B), where the spin-transfer torque dominates over the collective pinning of SkL, the above microscopic mechanism also qualitatively explains the experimental observation of the decrease of the nonlinear Hall signal above  $j_{CO}$ , which we assign to the onset of dynamical reordering (that is, onset of reduction of the effective pinning force). Because a stronger disorder potential yields a larger deformation of SkL, the nonlinear Hall signal is an increasing function of the strength of the pinning potential. Therefore, the effective reduction of the pinning force reduces

the deformation of skyrmion strings, leading to the decrease of non-linear Hall signals.

Finally, we discuss the nonreciprocal nonlinear Hall resistivity under DC density below  $j_c$  and in single-helix states (that is, helical and conical phases). In the former case, because the  $q_z$ -linear term in the response function, which is the source of nonreciprocity, enters only together with the dynamical term, the pinned skyrmions do not have the nonreciprocal term. Hence, the Hall electric field  $E_z^{\text{DC}}$  does not arise in the pinned regime below  $j_c$ , which is also consistent with experimental observations. In the single-helix state, because both  $e_z$  and  $b_y$  involve the derivative  $\partial_z$  along the magnetic field direction as seen from Eqs. 3 and 4, the nonreciprocal nature along the  $z$  direction is necessary. This effect is characteristic of SkL with a multiple- $\mathbf{Q}$  nature but is absent in the single-helix state. Hence, the Hall electric field  $E_z^{\text{DC}}$  is observed only for SkL.

We have demonstrated that the current-induced asymmetric deformation of skyrmion strings arising from both their flexible nature and the DM interaction results in a nonreciprocal transport response related to the real-space Berry phase of skyrmion strings. The asymmetric dynamics and the consequent nonreciprocal transport response are some of the generic properties of the dynamics of string-like objects in non-centrosymmetric systems, including vortex lines in noncentrosymmetric SCs as well as skyrmion strings in chiral magnets investigated here.

## MATERIALS AND METHODS

### Sample preparation

Single crystals of MnSi were synthesized by using the Czochralski method. Their crystalline chirality was confirmed by using the CBED method. Using the FIB technique (NB-5000, Hitachi), we cut the thin plates out of those single crystals. The dimensions of the thin plates were typically  $\sim 10 \mu\text{m} \times 10 \mu\text{m} \times 500 \text{nm}$ . The thin plates were mounted on a silicon stage and fixed by FIB-assisted tungsten deposition. The gold electrodes were patterned by combining photolithography and electron beam deposition techniques. We prepared several thin plates with left-handed and right-handed chirality in order to confirm reproducibility.

### Transport measurement

Linear longitudinal resistivity and planar Hall resistivity were measured by using the DC transport option of the Physical Property Measurement System. Second-harmonic resistivity was measured by using a lock-in technique (SR-830, Stanford Research Systems); we input low-frequency sine-wave AC and measured second-harmonic resistivity. To confirm the negligible effect of Joule heating, we simultaneously monitored the temperature by measuring longitudinal resistivity.

### Calculation of the nonreciprocal nonlinear Hall effect in SkL

We begin with the spin texture of the disordered SkL, which is given by superposing the three deformed helix states as (4, 7, 25)

$$\begin{aligned} \mathbf{n}(\mathbf{r}, t) &= \sum_{i=1}^3 \left[ \beta_i(\mathbf{r}, t) \hat{\mathbf{Q}}_i + \sqrt{1 - \beta_i(\mathbf{r}, t)^2} \mathbf{n}_i(\mathbf{r}, t) \right] \\ \mathbf{n}_i(\mathbf{r}, t) &= \hat{\mathbf{z}} \cos[\mathbf{Q}_i \cdot (\mathbf{r} - \mathbf{R}(t)) + \phi_i(\mathbf{r}, t)] + \\ &\quad \hat{\mathbf{Q}}_i \times \hat{\mathbf{z}} \sin[\mathbf{Q}_i \cdot (\mathbf{r} - \mathbf{R}(t)) + \phi_i(\mathbf{r}, t)] \end{aligned}$$

where  $\mathbf{Q}_{i=1,2,3}$  are modulation wave vectors of the helices perpendicular to the external magnetic field along the  $z$  direction. The low-energy

dynamics of SkL can be effectively described by the above dynamical phason field variables. The hat symbol represents a unit vector, and  $\hat{\mathbf{Q}}_1 = \left(-\frac{\sqrt{3}}{2}, -\frac{1}{2}, 0\right)$ ,  $\hat{\mathbf{Q}}_2 = \left(\frac{\sqrt{3}}{2}, -\frac{1}{2}, 0\right)$ , and  $\hat{\mathbf{Q}}_3 = (0, 1, 0)$ . The dy-

namical field variables  $\phi_i$  and  $\beta_i$  describe the deformation from the perfect lattice induced by the collision of spins with impurities. The phason field  $\phi_i$  shows the modulation of the phase of the helix, which is relevant to the low-energy dynamics of SkL, and its canonical conjugate variable  $\beta_i$  represents a tilt of spin moment from the plane perpendicular to  $\mathbf{Q}_i$ . The vector  $\mathbf{R}(t)$  is a uniform displacement driven by the external electrical current and has the form  $\mathbf{R}(t) = \mathbf{v}_{\text{Sk}} t$  in the DC limit.

Next, we consider the action for deformation field variables. The Berry phase term has the form (25, 30)

$$S_B = i\hbar \int dt \int \frac{d\mathbf{r}}{a^3} \sum_{ij} \left( \frac{9}{8} E_{ij} \phi_i \dot{\phi}_j - \frac{3}{2} P_{ij} \beta_i \dot{\beta}_j \right)$$

which describes the dynamics of spin texture. Here, we have introduced the symmetric and antisymmetric matrices by  $P_{ij} = \frac{2}{3} \hat{\mathbf{Q}}_i \cdot \hat{\mathbf{Q}}_j$  and  $E_{ij} = \frac{2}{3} \hat{\mathbf{z}} \cdot (\hat{\mathbf{Q}}_i \times \hat{\mathbf{Q}}_j)$ , respectively. We can consider the new phason field variables by  $\phi_x = \frac{1}{\sqrt{2}}(-\phi_1 + \phi_2)$ ,  $\phi_y = \frac{1}{\sqrt{6}}(-\phi_1 - \phi_2 + 2\phi_3)$ , and  $\phi_z = \frac{1}{\sqrt{3}}(\phi_1 + \phi_2 + \phi_3)$ , which correspond to two  $(x, y)$  translational modes and a massive breathing mode, respectively (25, 27). Similar quantities for  $\beta$  are also considered. We have neglected the massive breathing mode because the low-lying energy mode gives a dominant contribution. The above action is written only by translational modes, which is confirmed by rewriting the action in terms of  $\phi_{x,y,s}$  and  $\beta_{x,y,s}$ .

The action is then given by  $S = S_B - \int dt H$ , which determines the equation of motion and the response functions. The explicit form is written as

$$\begin{aligned} \phi_i(\mathbf{r}, t) &= \sum_j \int d\mathbf{r}' dt' G_{ij}(\mathbf{r} - \mathbf{r}', t - t') F_j(\mathbf{r}', t') \\ F_i(\mathbf{r}, t) &= \frac{2V(\mathbf{r})}{e^3} n^z(\mathbf{r}, t) \sin[\mathbf{Q}_i \cdot (\mathbf{r} - \mathbf{R}(t)) + \phi_i(\mathbf{r}, t)] \\ \beta_i(\mathbf{r}, t) &= \frac{3J\hbar}{2D^2} \sum_j \left( P_{ij} + \frac{3}{Q} E_{ij} \partial_z \right) \dot{\phi}_j(\mathbf{r}, t) \end{aligned}$$

Namely, the deformations  $\phi_i$  and  $\beta_i$  are generated from the impurity pinning force  $F_i$  through the response function  $G_{ij}$ . The term with the  $z$  derivative in the equation for the  $\beta$  field is responsible for the nonreciprocal nature of skyrmion strings. The Fourier-transformed Green function is given by

$$\begin{aligned} G_{ij}^{-1}(\mathbf{q}, \omega) &= \left( J a^2 \mathbf{q}^2 - \frac{9J\hbar^2}{4D^2} \omega^2 - i\lambda\hbar\omega \right) P_{ij} + \\ &\quad \left( \frac{9i\hbar}{4} \omega + \frac{27iJ^2\hbar^2 a}{4D^3} \omega^2 q_z \right) E_{ij} \end{aligned}$$

Here, we have introduced the damping term with the dimensionless coefficient  $\lambda$ . Because the low-energy dynamics is important at a small current density, we can neglect the high-order term with  $\omega^2$  and obtain the excitation energy as

$$\epsilon(\mathbf{q}) = \frac{4J a^2}{9} \mathbf{q}^2 - \frac{16J^3 a^4}{81D^2} \mathbf{q}^4 - \frac{16J^4 a^5}{27D^3} \mathbf{q}^4 q_z + O(q^6)$$

The quadratic dispersion at small  $\mathbf{q}$  originates from a topological property of SkL (30). The third term on the right-hand side with  $q_z$  shows nonreciprocal excitation. We note that the frequency  $\omega$  here corresponds to the excitation energy of SkL and is not related to the frequency  $f$  of the external current, which is used to measure second-harmonic resistivity, because we considered the DC limit (see also the Supplementary Materials for the relationship between the DC limit of the nonreciprocal nonlinear Hall effect, which we discussed theoretically, and second-harmonic resistivity).

We assume the spatially uncorrelated impurity potential with  $\langle V(\mathbf{r})V(\mathbf{r}') \rangle = V_{\text{imp}}^2 \ell^3 \delta(\mathbf{r} - \mathbf{r}')$ , where the angle bracket denotes the impurity average.  $V_{\text{imp}}$  can be written in terms of the critical current density ( $j_c$ ), and the final expression contains only  $j_c$ , as will be discussed later. We now consider the Hall electric field in the DC limit (see also Eqs. 3 to 5). Because  $\beta_i \propto \omega \phi_i$  from canonical conjugate relations, the terms that directly involve the phason field variables  $\phi_i$  are dominant at low frequencies, compared to contributions from  $\beta_i$  field variables. By expanding the expression with respect to deformation field variables, the leading-order contribution is given by

$$E_z^{\text{DC}} = \lim_{T \rightarrow \infty} \int_{-T}^T \frac{dt}{2T} \int \frac{d\mathbf{r}}{\Omega} P \langle (\mathbf{v}_e - \mathbf{v}_{\text{Sk}})_x b_y + e_z \rangle \\ \simeq \frac{P b_z}{3Q^2} \sum_{ijk} E_{ij} \lim_{T \rightarrow \infty} \int_{-T}^T \frac{dt}{2T} \int \frac{d\mathbf{r}}{\Omega} [\mathbf{Q}_i \cdot (\mathbf{v}_e - \mathbf{v}_{\text{Sk}}) + \partial_t \phi_i] \partial_z \phi_j \beta_k^2$$

In this equation, the emergent magnetic field  $b_y$  is of third-order with respect to the deformation field variables, and the emergent electric field  $e_z$  associated with dynamical internal deformation is the fourth-order term. We note that the second-order and first-order terms for  $e_z$  and  $b_y$  exist without integrating over space-time but vanish in the DC and uniform limit with negligible boundary contributions. A similar conclusion can be obtained if we consider the single skyrmion string (see the Supplementary Materials). Expanding the phason field with respect to the impurity potentials as  $\phi = \phi^{(1)} + \phi^{(2)} + O(V^3)$ , we now write the leading-order contribution for the Hall electric field in terms of the Fourier transposed variables as

$$E_1 = \left( \frac{v_e}{v_{\text{Sk}}} - 1 \right) E_1 + E_2 \\ - \frac{9iP\hbar\omega^*}{16e} \left( \frac{3J\hbar^2}{2D^2} \right)^2 \sum_{ijkl} E_{ij} \alpha_i \int \frac{d\mathbf{q}_1 d\mathbf{q}_2 d\mathbf{q}_3 d\omega_1 d\omega_2 d\omega_3}{(2\pi)^{12}} q_{1z} \omega_2 \omega_3 \times \\ \left( P_{kl} + \frac{6i}{Q} E_{kl} q_{3z} \right) \times [\langle \phi_j^{(2)}(\mathbf{q}_1, \omega_1) \phi_k^{(1)}(\mathbf{q}_2, \omega_2) \phi_l^{(1)}(\mathbf{q}_3, \omega_3) \rangle + \\ \langle \phi_j^{(1)}(\mathbf{q}_1, \omega_1) \phi_k^{(2)}(\mathbf{q}_2, \omega_2) \phi_l^{(1)}(\mathbf{q}_3, \omega_3) \rangle + \\ \langle \phi_j^{(1)}(\mathbf{q}_1, \omega_1) \phi_k^{(1)}(\mathbf{q}_2, \omega_2) \phi_l^{(2)}(\mathbf{q}_3, \omega_3) \rangle] \\ E_2 = - \frac{9P\hbar}{16e} \left( \frac{3J\hbar^2}{2D^2} \right)^2 \sum_{ijkl} E_{ij} \int \frac{d\mathbf{q}_1 d\mathbf{q}_2 d\mathbf{q}_3 d\mathbf{q}_4 d\omega_1 d\omega_2 d\omega_3 d\omega_4}{(2\pi)^{16}} \omega_1 q_{2z} \omega_3 \omega_4 \times \\ \left( P_{kl} + \frac{6i}{Q} E_{kl} q_{4z} \right) \langle \phi_i^{(1)}(\mathbf{q}_1, \omega_1) \phi_j^{(1)}(\mathbf{q}_2, \omega_2) \phi_k^{(1)}(\mathbf{q}_3, \omega_3) \phi_l^{(1)}(\mathbf{q}_4, \omega_4) \rangle$$

where  $\alpha_i = \hat{\mathbf{v}}_{\text{Sk}} \cdot \hat{\mathbf{Q}}_i$ . We have defined  $\omega^* = Q v_{\text{Sk}}$ , which is the characteristic frequency for moving skyrmions corresponding to the

periodic passage of the “washboard potential” of SkL. These are evaluated with the conservation laws of momentum and energy which naturally enter through Fourier transformation. The contributions  $E_1$  and  $E_2$  are those from emergent fields  $b_y$  and  $e_z$  in the moving frame, respectively. The contributions from both  $e_z$  and  $b_y$  are of fourth-order with respect to  $V_{\text{imp}}$  and have the same parameter dependence. Hence, these can be of the same orders of magnitude, which are numerically shown later. Keeping the  $q_z$ -linear term in the lowest order, we obtain the leading-order contribution for the Hall electric field as

$$E_z^{\text{DC}} \simeq \frac{243PD}{512ea} \left( \frac{a}{\ell} \right)^6 \left( \frac{V_{\text{imp}}}{J} \right)^4 \frac{(\hbar\omega_0^*)^3}{|D|^3} \left[ \left( \frac{v_e}{v_{\text{Sk}}} - 1 \right) f_b(\lambda) + f_e(\lambda) \right]$$

We have defined  $\omega_0^* = \frac{J}{D} \omega^* = v_{\text{Sk}}/a$ . The dimensionless functions  $f_b(\lambda)$  and  $f_e(\lambda)$  represent contributions from emergent magnetic and electric fields in the moving frame, respectively, and can be evaluated by performing the  $\mathbf{q}$ -integrals of products of four Green functions. Figure S1 shows the damping coefficient  $\lambda$  dependences of  $f_b(\lambda)$  and  $f_e(\lambda)$ . For weak impurities, assuming that the damping coefficient  $\lambda$  for the moving regime near  $j_c$  has a characteristic similar to the one in the pinned regime with  $j < j_c$ , we can use the relation  $\lambda \sim 1$  derived for pinned SkL, and then the function  $f_{e,b}(\lambda) \sim f_{e,b}(1)$  can be regarded as a constant on the order of unity. We have thus confirmed that these functions can be of the same orders of magnitude. Because the signs are not unique, the Hall electric field can be either negative or positive depending on the form of disorder potentials.

For comparison, we have also checked another form of the impurity potential. Namely, we choose the random Ising field  $H_{\text{imp}} = \int \frac{d\mathbf{r}}{\ell^3} V(\mathbf{r}) n^z$  instead of random anisotropy. While the parameter dependences (such as  $\omega^*$ ,  $V_{\text{imp}}$ ,  $J$ , and  $D$ ) of the Hall electric field are the same, the values of dimensionless functions  $f_b(\lambda)$  and  $f_e(\lambda)$  are nearly  $10^3$  times smaller than those for random anisotropy. Hence, the value of the Hall signal is sensitively dependent on the types of the impurity potentials.

Let us relate the pinning potential to the critical current density. The energy supplied to the spin texture through spin transfer torque is given by  $H_{\text{ext}} = P b_z \int d\mathbf{r} j_x u_y$ , where  $u_y = (-\phi_1 - \phi_2 + 2\phi_3)/Q$  is a displacement along the  $y$  direction (30). This energy is set as equal to the pinning energy at the critical current density (31). For the weak pinning case, the SkL is collectively pinned by impurities in the range over the pinning length  $\xi_p \sim a \left( \frac{J}{V_{\text{imp}}} \right)^2 \left( \frac{\ell}{a} \right)^3$ . The relation for the energy density balance is

$$\frac{P b_z j_c}{Q} \sim \frac{\sqrt{V_{\text{imp}}^2 (\xi_p/\ell)^3}}{\xi_p^3}$$

which shows  $j_c \propto V_{\text{imp}}^4$ . Rewriting the impurity pinning potential at the critical current density and noting the magnitude relation  $v_{\text{Sk}} \lesssim v_e$ , we obtained Eq. 6.

## SUPPLEMENTARY MATERIALS

Supplementary material for this article is available at <http://advances.sciencemag.org/cgi/content/full/4/8/eaat1115/DC1>

Section S1. Determination of the magnetic phase diagram for MnSi thin plates

Section S2. Relationship between the nonreciprocal nonlinear Hall effect and second-harmonic resistivity

Section S3. Current dependence of the nonlinear Hall effect measured by using square-wave current

Section S4. Frequency dependence of skyrmion velocity

Section S5. Calculation of nonreciprocal nonlinear Hall responses to AC  
 Section S6. Calculation of current-induced dynamics of a single skyrmion string  
 Fig. S1. Functional forms of the dimensionless functions  $f_b(\lambda)$  and  $f_c(\lambda)$ .  
 Fig. S2. Temperature dependence of longitudinal resistivity and magnetic field dependence of planar Hall resistivity.  
 Fig. S3. Current dependence of the nonreciprocal nonlinear Hall effect measured by using square-wave current.  
 Fig. S4. Frequency dependence of skyrmion velocity.  
 References (32–34)

## REFERENCES AND NOTES

- N. D. Mermin, The topological theory of defects in ordered media. *Rev. Mod. Phys.* **51**, 591–648 (1979).
- G. Blatter, M. V. Feigel'man, V. B. Geshkenbein, A. I. Larkin, V. M. Vinokur, Vortices in high-temperature superconductors. *Rev. Mod. Phys.* **66**, 1125–1388 (1994).
- M.-B. Luo, X. Hu, Depinning and creep motion in glass states of flux lines. *Phys. Rev. Lett.* **98**, 267002 (2007).
- S. Mühlbauer, B. Binz, F. Jonietz, C. Pfleiderer, A. Rosch, A. Neubauer, R. Georgii, P. Böni, Skyrmion lattice in a chiral magnet. *Science* **323**, 915–919 (2009).
- X. Z. Yu, Y. Onose, N. Kanazawa, J. H. Park, J. H. Han, Y. Matsui, N. Nagaosa, Y. Tokura, Real-space observation of a two-dimensional skyrmion crystal. *Nature* **465**, 901–904 (2010).
- H. S. Park, X. Yu, S. Aizawa, T. Tanigaki, T. Akashi, Y. Takahashi, T. Matsuda, N. Kanazawa, Y. Onose, D. Shindo, A. Tonomura, Y. Tokura, Observation of the magnetic flux and three-dimensional structure of skyrmion lattices by electron holography. *Nat. Nanotechnol.* **9**, 337–342 (2014).
- N. Nagaosa, Y. Tokura, Topological properties and dynamics of magnetic skyrmions. *Nat. Nanotechnol.* **8**, 899–911 (2013).
- N. Kanazawa, S. Seki, Y. Tokura, Noncentrosymmetric magnets hosting magnetic skyrmions. *Adv. Mater.* **29**, 1603227 (2017).
- A. Neubauer, C. Pfleiderer, B. Binz, A. Rosch, R. Ritz, P. G. Niklowitz, P. Böni, Topological Hall effect in the A phase of MnSi. *Phys. Rev. Lett.* **102**, 186602 (2009).
- F. Jonietz, S. Mühlbauer, C. Pfleiderer, A. Neubauer, W. Münzer, A. Bauer, T. Adams, R. Georgii, P. Böni, R. A. Duine, K. Everschor, M. Garst, A. Rosch, Spin transfer torques in MnSi at ultralow current densities. *Science* **330**, 1648–1651 (2010).
- T. Schulz, R. Ritz, A. Bauer, M. Halder, M. Wagner, C. Franz, C. Pfleiderer, K. Everschor, M. Garst, A. Rosch, Emergent electrodynamics of skyrmions in a chiral magnet. *Nat. Phys.* **8**, 301–304 (2012).
- A. Fert, V. Cros, J. Sampaio, Skyrmions on the track. *Nat. Nanotechnol.* **8**, 152–156 (2013).
- J. Iwasaki, M. Mochizuki, N. Nagaosa, Universal current-velocity relation of skyrmion motion in chiral magnets. *Nat. Commun.* **4**, 1463 (2013).
- S.-Z. Lin, A. Saxena, Dynamics of Dirac strings and monopolelike excitations in chiral magnets under a current drive. *Phys. Rev. B* **93**, 060401(R) (2016).
- K. Garello, I. M. Miron, C. O. Avci, F. Freimuth, Y. Mokrousov, S. Blügel, S. Auffret, O. Boulle, G. Gaudin, P. Gambardella, Symmetry and magnitude of spin-orbit torques in ferromagnetic heterostructures. *Nat. Nanotechnol.* **8**, 587–593 (2013).
- K. Tsuda, M. Tanaka, Refinement of crystal structural parameters using two-dimensional energy-filtered CBED patterns. *Acta Crystallogr. A* **55**, 939–954 (1999).
- T. Yokouchi, N. Kanazawa, A. Kikkawa, D. Morikawa, K. Shibata, T. Arima, Y. Taguchi, F. Kagawa, Y. Tokura, Electrical magnetochiral effect induced by chiral spin fluctuations. *Nat. Commun.* **8**, 866 (2017).
- R. M. Fleming, C. C. Grimes, Sliding-mode conductivity in NbSe<sub>3</sub>: Observation of a threshold electric field and conduction noise. *Phys. Rev. Lett.* **42**, 1423–1426 (1979).
- G. Grüner, The dynamics of charge-density waves. *Rev. Mod. Phys.* **60**, 1129–1181 (1988).
- U. Yaron, P. L. Gammel, D. A. Huse, R. N. Klemiman, C. S. Oglesby, E. Bucher, B. Batlogg, D. J. Bishop, K. Mortensen, K. N. Clausen, Structural evidence for a two-step process in the depinning of the superconducting flux-line lattice. *Nature* **376**, 753–755 (1995).
- C. J. Olson, C. Reichhardt, F. Nori, Nonequilibrium dynamic phase diagram for vortex lattices. *Phys. Rev. Lett.* **81**, 3757–3760 (1998).
- C. Reichhardt, D. Ray, C. J. O. Reichhardt, Collective transport properties of driven skyrmions with random disorder. *Phys. Rev. Lett.* **114**, 217202 (2015).
- K. Yasuda, A. Tsukazaki, R. Yoshimi, K. Kondou, K. S. Takahashi, Y. Otani, M. Kawasaki, Y. Tokura, Current-nonlinear Hall effect and spin-orbit torque magnetization switching in a magnetic topological insulator. *Phys. Rev. Lett.* **119**, 137204 (2017).
- W. Kleemann, J. Rhensius, O. Petracic, J. Ferré, J. P. Jamet, H. Bernas, Modes of periodic domain wall motion in ultrathin ferromagnetic layers. *Phys. Rev. Lett.* **99**, 097203 (2007).
- G. Tataru, H. Fukuyama, Phonons and excitations in skyrmion lattice. *J. Phys. Soc. Jpn.* **83**, 104711 (2014).
- P. Bak, M. H. Jensen, Theory of helical magnetic structures and phase transitions in MnSi and FeGe. *J. Phys. C* **13**, L881 (1980).
- S. Hoshino, N. Nagaosa, Theory of the magnetic skyrmion glass. *Phys. Rev. B* **97**, 024413 (2018).
- G. E. Volovik, *The Universe in a Helium Droplet* (Oxford Univ. Press, 2003).
- N. Nagaosa, Y. Tokura, Emergent electromagnetism in solids. *Phys. Scr.* **T146**, 014020 (2012).
- J. Zang, M. Mostovoy, J. H. Han, N. Nagaosa, Dynamics of Skyrmion crystals in metallic thin films. *Phys. Rev. Lett.* **107**, 136804 (2011).
- P. A. Lee, T. M. Rice, Electric field depinning of charge density waves. *Phys. Rev. B* **19**, 3970–3980 (1979).
- A. E. Petrova, V. N. Krasnorussky, T. A. Lograsso, S. M. Stishov, High-pressure study of the magnetic phase transition in MnSi. *Phys. Rev. B* **79**, 100401(R) (2009).
- A. A. Thiele, Steady-state motion of magnetic domains. *Phys. Rev. Lett.* **30**, 230–233 (1973).
- F. Büttner, C. Moutafis, M. Schneider, B. Krüger, C. M. Günther, J. Geilhufe, C. v. K. Schmising, J. Mohanty, B. Pfau, S. Schaffert, A. Bisig, M. Foerster, T. Schulz, C. A. F. Vaz, J. H. Franken, H. J. M. Swagten, M. Kläui, S. Eisebitt, Dynamics and inertia of skyrmionic spin structures. *Nat. Phys.* **11**, 225–228 (2015).

**Acknowledgments:** We appreciate Y. Okamura, K. Yasuda, and W. Koshibae for useful discussions. **Funding:** This work was supported by the Japan Society for the Promotion of Science (JSPS) KAKENHI (grant nos. 26103006, 18H03676, 24226002, and 15H05456) and Core Research for Evolutional Science and Technology (CREST), Japan Science and Technology Agency (JST) (grant no. JPMJCR16F1). **Author contributions:** N.N. and Y. Tokura conceived the whole project. T.Y. fabricated thin-plate samples with assistance from K.S. and conducted transport measurements. S.H. carried out the theoretical calculations. A.K. grew single crystals. D.M. carried out CBED. N.K., T.A., Y. Taguchi, F.K., N.N., and Y. Tokura supervised the project. T.Y., S.H., N.N., and Y. Tokura wrote the draft. All authors discussed the results and commented on the manuscript. **Competing interests:** The authors declare that they have no competing interests. **Data and materials availability:** All data needed to evaluate the conclusions in the paper are present in the paper and/or the Supplementary Materials. Additional data related to this paper may be requested from the authors.

Submitted 24 January 2018

Accepted 29 June 2018

Published 10 August 2018

10.1126/sciadv.aat1115

**Citation:** T. Yokouchi, S. Hoshino, N. Kanazawa, A. Kikkawa, D. Morikawa, K. Shibata, T. Arima, Y. Taguchi, F. Kagawa, N. Nagaosa, Y. Tokura, Current-induced dynamics of skyrmion strings. *Sci. Adv.* **4**, eaat1115 (2018).